A three-dimensional spectral boundary element algorithm for interfacial dynamics in Stokes flow

Yechun Wang and P. Dimitrakopoulos[a)]
Department of Chemical and Biomolecular Engineering, University of Maryland, College Park, Maryland 20742

(Received 16 May 2006; accepted 25 July 2006; published online 31 August 2006)

In the present study we describe a novel three-dimensional spectral boundary element algorithm for interfacial dynamics in Stokes flow and/or gravity. The main attraction of this approach is that it exploits all the benefits of the spectral methods (i.e., exponential convergence and numerical stability) with the versatility of the finite element method. In addition, it is not affected by the disadvantage of the spectral methods used in volume discretization to create denser systems. Our algorithm also exploits all the benefits of the boundary element techniques, i.e., a reduction of the problem dimensionality and great parallel scalability. To achieve continuity of the interfacial geometry and its derivatives at the edges of the spectral elements during the droplet deformation, a suitable interfacial smoothing is developed based on a Hermitian-like interpolation. An adaptive mesh reconstructing procedure based on the relevant lengths of the spectral elements is also described. In addition, we consider the inertialess motion of a buoyant droplet left to rise (or sediment) near a vertical solid wall and compare our numerical results with analytical predictions. In our study we emphasize the need for computational studies for the accurate determination of droplet migration near solid walls. © *2006 American Institute of Physics*.
[DOI: 10.1063/1.2337572]

I. INTRODUCTION

The dynamics of droplets and bubbles in infinite media or in restricted geometries under viscous flows and/or gravity is a problem of great technological and fundamental interest since it is encountered in a broad range of industrial, natural, and physiological processes. Industrial applications include enhanced oil recovery, coating operations, vapor condensation, waste treatment, advanced material processing, and microfluidic devices. Pharmaceutical applications include emulsions that serve as a vehicle for the transport of the medical agent through the skin. One further application constitutes the blood flow in microvessels.

Since the pioneering work of Youngren and Acrivos[1] nearly 30 years ago, interfacial dynamics in Stokes flow via the solution of boundary integral equations has developed considerably. The main benefits of this approach are the reduction of the problem dimensionality by one and the great parallel scalability. Much research has been done to determine and understand the deformation of droplets and bubbles in external flows, both in infinite media as well as in constrained geometries.[2–4] Considerable progress has also been made in the study of membrane-like interfaces, such as those in artificial capsules and biological cells.[4,5] During the last few years, the interaction of deformable interfaces, e.g., suspensions of droplets, has received a lot of interest.[6] To study these problems, several numerical methodologies have been developed based on low-order interpolation schemes; e.g., see Refs. 4 and 7–10.

In the present paper we develop a spectral boundary element algorithm for interfacial dynamics in Stokes flow. The main attraction of our high-order algorithm is that it exploits all the benefits of the spectral methods (i.e., exponential convergence and numerical stability as the number of discretization points increases) with the versatility of the finite element method, i.e., the ability to handle the most complicated geometries, such as those for interfacial motion in porous media or microfluidics.[11–13] In addition, it is not affected by the disadvantage of the spectral methods used in volume discretization; namely, the requirement to deal with dense systems, because in boundary integral formulations the resulting systems are always dense, independent of the form of discretization. Our method also exploits all the benefits of the boundary element techniques, i.e., a reduction of the problem dimensionality and great parallel scalability.

We emphasize that robust spectral boundary element algorithms have been developed for the study of fixed boundary surfaces,[14–16] particulate flows,[17] and equilibrium interfaces under steady flows and/or gravity.[18–22] Therefore, with the present algorithm we seek to extend the spectral boundary element formulation to the problem of interfacial dynamic evolution.

After the mathematical formulation in Sec. II, in Sec. III we present the spectral interfacial discretization. By applying a time advancing scheme, the resulting algorithm is numerically unstable due to discontinuities at the edges of the spectral elements. To avoid the growth of these numerical discrepancies, in Sec. IV we develop a suitable interfacial smoothing based on a Hermitian-like interpolation that preserves the continuity of the interfacial geometry and its derivatives at the edges of the spectral elements during the droplet deformation. In Sec. V we present the major property

[a)]Electronic mail: dimitrak@eng.umd.edu

of our interfacial algorithm, i.e., the exponential convergence in the numerical accuracy as the number of the employed spectral points increases. An adaptive mesh reconstructing procedure based on the relevant lengths of the spectral elements is also described. Our numerical results are in excellent agreement with experimental findings, analytical predictions, and previous numerical computations in a wide array of different flows and viscosity ratios.

In Sec. VI we apply our numerical algorithm to study the inertialess motion of a buoyant droplet left to rise (or sediment) near a vertical solid wall. We investigate the (initial) transient effects on the droplet motion while we also compare our numerical results with the quasisteady analytical predictions of Magnaudet, Takagi, and Legendre.[23] Our study demonstrates that the analytical model underestimates the migration velocity away from the wall or erroneously predicts lateral motion toward the solid wall for viscosity ratio $\lambda = O(1)$ and Bond number $B_d = O(1)$. Thus, our work emphasizes the need for computational studies for the accurate determination of droplet migration near solid walls.

II. MATHEMATICAL FORMULATION

We consider a three-dimensional droplet suspended in an infinite fluid; the droplet (fluid 1) has density ρ_1 and viscosity $\lambda\mu$, while the surrounding fluid (fluid 2) has density ρ_2 and viscosity μ. The droplet size is specified by its volume V or equivalently by the radius a of a spherical droplet of volume $4\pi a^3/3 = V$. The gravitational acceleration is g while the surface tension γ is assumed constant. Far from the droplet, the flow approaches the undisturbed flow $\boldsymbol{u}^\infty$, e.g., a planar extensional flow $\boldsymbol{u}^\infty = G(x,-y,0)$ or a simple shear flow $\boldsymbol{u}^\infty = G(z,0,0)$, where G is the shear rate. In this study, the characteristic length a is used as the length scale while the time is scaled with the flow time scale G^{-1}.

The capillary number Ca and Bond number B_d are defined by

$$\mathrm{Ca} = \frac{\mu G a}{\gamma}, \quad B_d = \frac{(\rho_2 - \rho_1) g a^2}{\gamma}. \tag{1}$$

These dimensionless parameters represent the ratio of viscous flow forces and gravitational forces to interfacial forces, respectively.

The governing equations in fluid 2 are the Stokes equations together with continuity,

$$\boldsymbol{\nabla} \cdot \boldsymbol{\sigma} = -\boldsymbol{\nabla} p + \mu \nabla^2 \boldsymbol{u} = 0, \tag{2}$$

$$\boldsymbol{\nabla} \cdot \boldsymbol{u} = 0, \tag{3}$$

while in the droplet the same equations apply, with the viscosity replaced by $\lambda\mu$.

At the interface, the boundary conditions on the velocity $\boldsymbol{u}$ and surface stress $\boldsymbol{f}$ are

$$\boldsymbol{u}_1 = \boldsymbol{u}_2, \tag{4}$$

$$\Delta \boldsymbol{f} = \boldsymbol{f}_2 - \boldsymbol{f}_1 = \gamma(\boldsymbol{\nabla} \cdot \boldsymbol{n})\boldsymbol{n} + (\rho_2 - \rho_1)(\boldsymbol{g} \cdot \boldsymbol{x})\boldsymbol{n}. \tag{5}$$

Here the subscripts designate quantities evaluated in fluids 1 and 2, respectively. The surface stress is defined as $\boldsymbol{f} = \boldsymbol{\sigma} \cdot \boldsymbol{n}$, where $\boldsymbol{n}$ is the unit normal that we choose to point into fluid 2. The pressure as defined in $\boldsymbol{\sigma}$ is the dynamic pressure; hence the gravity force is absent from Eq. (2) and appears in the interfacial stress boundary condition, Eq. (5).

For a given droplet surface, S_B, the velocity at a point $\boldsymbol{x}_0$ on the interface may be determined via the boundary integral equation,[24]

$$(1+\lambda)\boldsymbol{u}(\boldsymbol{x}_0) - 2\boldsymbol{u}^\infty(\boldsymbol{x}_0) = -\frac{1}{4\pi\mu}\int_{S_B} [\boldsymbol{S} \cdot \Delta \boldsymbol{f} - (1-\lambda)\mu \boldsymbol{T} \cdot \boldsymbol{u} \cdot \boldsymbol{n}](\boldsymbol{x}) dS, \tag{6}$$

where S_{ij} is the fundamental solution for the three-dimensional Stokes equations and T_{ijk} is the associated stress defined by

$$S_{ij} = \frac{\delta_{ij}}{r} + \frac{\hat{x}_i \hat{x}_j}{r^3}, \quad T_{ijk} = -6\frac{\hat{x}_i \hat{x}_j \hat{x}_k}{r^5}, \tag{7}$$

where $\hat{\boldsymbol{x}} = \boldsymbol{x} - \boldsymbol{x}_0$ and $r = |\hat{\boldsymbol{x}}|$.[24] Similar equations hold in the presence of solid boundaries and for drop suspensions.[6,19]

The time evolution of the interfacial shape may be determined via the kinematic condition at the interface,

$$\frac{\mathrm{d}\boldsymbol{x}}{\mathrm{d}t} = (\boldsymbol{u} \cdot \boldsymbol{n})\boldsymbol{n}. \tag{8}$$

Although the governing equations and boundary conditions are linear in $\boldsymbol{u}$ and $\boldsymbol{f}$, the problem of determining the dynamic droplet shape constitutes a nonlinear problem, i.e., the velocity $\boldsymbol{u}$, stress $\boldsymbol{f}$, and curvature $\boldsymbol{\nabla} \cdot \boldsymbol{n}$ are nonlinear functions of the geometrical variables describing the interface shape.

III. NUMERICAL METHOD

A. Spectral boundary discretization

The numerical solution of the boundary integral equation, Eq. (6), is achieved through an extension of the spectral boundary element method.[14,15] The initial interface is divided into a moderate number N_E of curvilinear quadrilateral elements, as shown in Fig. 1. We note that one may describe the drop interface in a global coordinate system in terms of spectral expansions without the need for an element discretization. However, by employing elements, calculations via interpolation are more efficient since they are based on the spectral points defined on each element (and not on the entire interface). We also have the ability to concentrate the spectral points in portion(s) of the interface we need most during the interfacial evolution (see Sec. V B). In addition, complicated solid geometries can be handled easily via element discretization for studies of droplet dynamics in confined geometries, e.g., porous media and microfluidics.

Since we employ quadrilateral elements, a convenient way of discretizing the initial spherical interface is via cube projection, i.e., the surface of the drop is projected onto a cube whose faces correspond to the interfacial elements. While we have the ability to project the initial geometry into any prism and divide the prism's faces into additional elements, we have found that it is more efficient (as well as a more general approach) to discretize the initial spherical interface into six equal-size elements (as the ones shown in

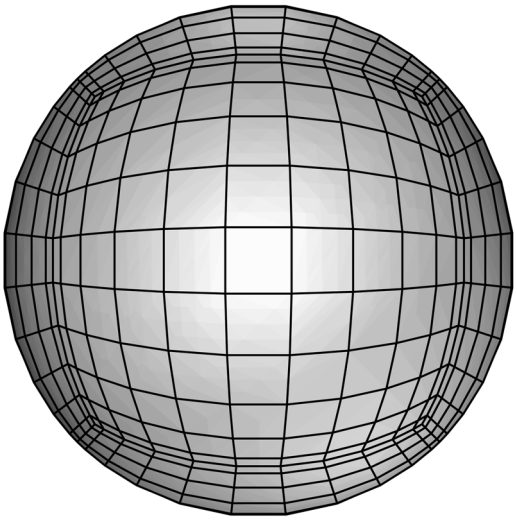

FIG. 1. Spectral boundary element discretization of a spherical droplet into $N_E=6$ elements. The figure illustrates a Gauss-Lobatto Legendre distribution of nodal lines with $N_B=12$ spectral points in each direction.

Fig. 1) and rely on our adaptive mesh reconstruction algorithm (presented later in Sec. V B) to derive additional elements during the interfacial evolution. However, if the initial geometry is an elongated shape (e.g., a spheroid) more than six elements may be employed to account for the interfacial elongation. More details on the surface element discretization may be found in Muldowney and Higdon.[15]

The geometric variables on each element are discretized using Lagrangian interpolation in terms of parametric variables ξ, η on the square interval $[-1,1]^2$, e.g.,

$$\boldsymbol{x}(\xi,\eta)=\sum_{i=1}^{N_B}\sum_{j=1}^{N_B}\boldsymbol{x}(\xi_i,\eta_j)h_i(\xi)h_j(\eta), \tag{9}$$

where h_i is the (N_B-1)-order Lagrangian interpolant polynomial. The physical variables $\boldsymbol{u}$ and $\boldsymbol{f}$ are represented similarly. The base points (ξ_i,η_j) for the interpolation are chosen as the zeros of N_B-order orthogonal polynomials. This is equivalent to an orthogonal polynomial expansion and yields the spectral convergence associated with such expansions.

The boundary integral equation, Eq. (6), admits two different types of points. The collocation points $\boldsymbol{x}_0$ of the left-hand side where the equation is required to hold and the basis points $\boldsymbol{x}$ of the right-hand side where the physical variables $\boldsymbol{u}$ and $\boldsymbol{f}$ are defined. The spectral element method as implemented here employs collocation points of Gauss quadrature, i.e., in the interior of the element. As a result the boundary integral equation holds even for singular elements, where the normal vector is not uniquely defined. In addition, we use basis points of the Gauss-Lobatto quadrature[11] that facilitate the interfacial smoothing described later in Sec. IV.

The Gauss-type points may be derived from the Jacobi polynomials $P_N^{\alpha,\beta}$, where the parametric constants α and β are greater than -1.[11,25] Different values of α and β yield diverse orthogonal polynomials, e.g., $\alpha=\beta=0$ yields the Legendre polynomials while $\alpha=\beta=-1/2$ produces the Chebyshev polynomials. Similar to the interior Gauss points, Gauss-Lobatto points (which include the end points ±1) can also be derived from the Jacobi polynomials; the distribution of the interior points is again controlled by the associated parameters α and β. Note that equal values of the two parameters, α and β, result in points symmetric around zero in the interval $[-1,1]$. As the value of $\alpha=\beta$ approaches -1, the roots are closer to the ends of the interval; larger values produce roots closer to the center of the interval $[-1,1]$ (see Fig. 2). Thus, by choosing different values of $\alpha=\beta$, we can change the distribution of the basis points. This distribution can also be controlled by employing appropriate stretching functions.

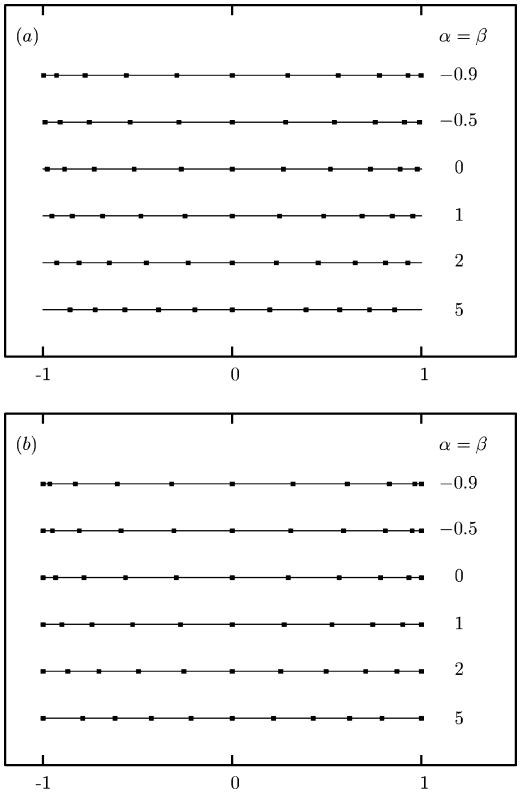

FIG. 2. The distribution in $[-1,1]$ of $N_B=11$ roots of Jacobi polynomials for $\alpha=\beta=-0.9,-0.5,0,1,2,5$. (a) Gauss points. (b) Gauss-Lobatto points.

The discretized expressions for the geometry and the physical variables are substituted into the boundary integral equations yielding a linear system of algebraic equations $\boldsymbol{u}=\boldsymbol{Af}+\boldsymbol{Bu}$. The system matrices $\boldsymbol{A}$ and $\boldsymbol{B}$ are defined as integrals of the kernels $\boldsymbol{S}$ and $\boldsymbol{T}$ and the basis functions over the set of the surface elements. The numerical integration is performed by Gauss-Legendre quadrature with the aid of variable transformations as described in Ref. 15. We emphasize that to achieve the accuracy reported in this paper, the integration error should be smaller than the error associated with the time step and the spectral interpolation.

Our numerical code has been parallelized on shared-memory multiprocessor computers (such as the SGI Origin 2000) by employing Open MP directives for the calculation of the system matrix, and highly optimized parallel routines from the LAPACK system library for the solution of the dense system matrix. Multiprocessor runs exploit the parallel nature of calculating the system matrices, resulting in a nearly linear decrease in c.p.u. time. Thus, we have the abil-

ity to utilize the computational power available at supercomputer centers, including the National Center for Supercomputing Applications (NCSA) in Illinois. This facilitates considerably the study of a wide range of complicated problems involving fully three-dimensional interfaces in Stokes flow and/or gravity.

B. Explicit time-integration algorithm

In order to determine the shape of the drop as a function of time, an explicit time-integration algorithm is employed to solve the kinematic condition at the interface in the form

$$\frac{d\boldsymbol{x}}{dt} = (\boldsymbol{u}\cdot\boldsymbol{n})\boldsymbol{n} + U_t\boldsymbol{t}, \tag{10}$$

where the first term on the right-hand side denotes the contribution of the normal interfacial velocity while the second term denotes the contribution of some velocity tangential to the interface. (Note that $\boldsymbol{t}$ is a unit tangent vector to the interface). The interfacial shape is dictated by the normal interfacial velocity; the tangential velocity is employed to produce an even distribution of the spectral points (as well as an even size of the spectral elements) during the time evolution of the interface, as commonly occurs with other boundary integral implementations, e.g., Refs. 8–10 and 26.

An explicit Runge-Kutta method is employed for the time integration of Eq. (10) at the Gauss-Lobatto basis points, where the interfacial velocity $\boldsymbol{u}$ is determined. The time step Δt should be sufficiently small to ensure numerical stability, the well-known Courant condition, which in dimensionless form may be written as

$$\Delta t < O(\mathrm{Ca}\,\Delta x_{\min}), \tag{11}$$

where $\Delta x_{\min}$ is the minimum length scale appearing in the computational problem, e.g., the minimum grid spacing or the distance between interfaces in close contact.[7–9,27,28] (For gravity-only induced deformation, the time step should be reduced as the Bond number decreases.[29]) We emphasize that the Courant condition is associated with the explicit nature of the time integration and thus it is independent of the type of interfacial discretization. On the other hand, due to its high accuracy, our method may not require as dense a numerical grid as low-order boundary element methods, and thus the required time step may be higher.

If we apply the advancing scheme described above without any (additional) geometric constraints, the resulting algorithm is unstable, as shown in Fig. 3 for a droplet in a planar extensional flow with $\mathrm{Ca}=0.2$ and $\lambda=0.01$. The numerical instability is caused by the discontinuity at the edges of the spectral elements shown in Fig. 3(b). In particular, starting from an initial smooth interfacial shape, the geometry derived by the time integration of Eq. (10) above shows discrepancies at the edges of the spectral elements. These discrepancies are caused by differences in the numerical accuracy across neighbor spectral elements and thus they are very small after one or a few time steps but may grow substantially with time if left unattended. Note that in this figure we enforce coincidence of the Gauss-Lobatto basis points at the edges of the spectral elements; thus the geometry is always continuous across the spectral elements. On the other hand, the derivatives of the interfacial geometry, e.g., the tangent/normal vectors and the curvature, are not continuous across the spectral elements, as clearly shown in Fig. 3(b). To avoid the growth of the numerical discrepancies at the edges of the spectral elements, we smooth the interfacial geometry at the end of each time step, as discussed in the next session.

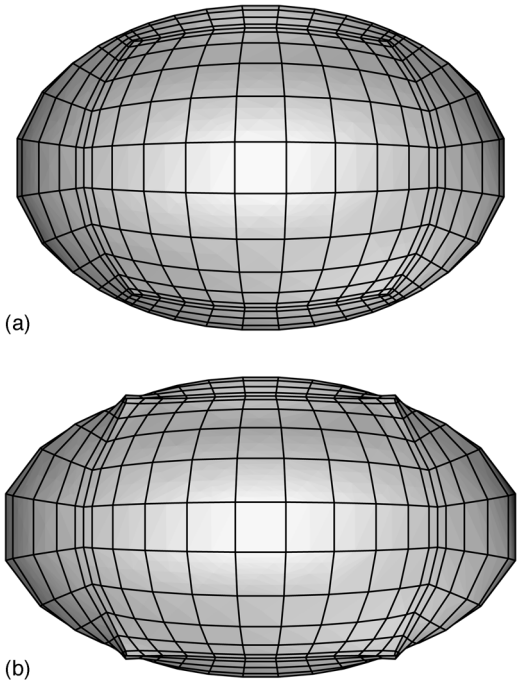

FIG. 3. Time evolution of a droplet in a planar extensional flow for $\mathrm{Ca}=0.2$ and $\lambda=0.01$. A fourth-order Runge-Kutta (RK4) scheme without interfacial smoothing is employed with $N_E=6$, $N_B=12$, and $\Delta t=2\times10^{-3}$. The droplet shape is shown for (a) time $t=0.18$, i.e., step $N_{\mathrm{step}}=90$, and (b) time $t=0.28$ or $N_{\mathrm{step}}=140$. The droplet initial shape is shown in Fig. 1. For this specific case, the interfacial shape breaks at time step $N_{\mathrm{step}}=156$.

IV. INTERFACIAL SMOOTHING

Our first-order smoothing scheme presented here eliminates the discrepancy in the position, the tangent, and the normal vectors at the edges across the spectral elements appearing during the interfacial deformation. The smoothing process involves two stages: first we smooth the geometry and its first derivatives at the element edges, and then we update the position of all points on each spectral element by employing a suitable Hermitian-like interpolation.

Let the nonsmoothed interfacial shape of the Gauss-Lobatto basis points at time $t+\Delta t$, derived by the time integration of Eq. (10) above, be identified as $\boldsymbol{x}^{\mathrm{old}}(\xi,\eta)$, where ξ and η are the two parametric variables describing the interface. At each spectral point at the element ends we define a local Cartesian coordinate system $\boldsymbol{x}^L$ with the x_1^L and x_2^L axes in the tangent plane and the x_3^L axis parallel to the normal vector $\boldsymbol{n}$. (One of the two local tangent coordinates, x_1^L and x_2^L, is taken to be parallel to the element edge we want to smooth.) A specific geometry is illustrated in Fig. 4, where the points a and b are two coincident points belonging to the consecutive elements A and B, respectively. The solid arrows represent the curvilinear coordinates (ξ,η) and the dashed

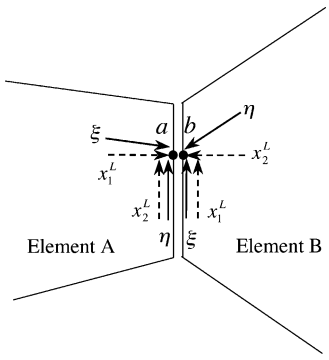

FIG. 4. An illustration for the curvilinear coordinates (ξ,η) and the local Cartesian coordinates (x_1^L,x_2^L). The spectral points a and b are two coincident points belonging to the consecutive spectral elements A and B, respectively.

arrows the local Cartesian coordinates (x_1^L,x_2^L). (The normal vector $\boldsymbol{n}$ and the third local Cartesian coordinate x_3^L are not plotted.) In the illustrated geometry, the parametric variable η at the point a coincides with the variable ξ at the point b while they both point at the same direction. We note that, due to the surface discretization, other combinations are possible, e.g., the coordinate ξ at the point a may coincide with the coordinate ξ at the point b pointing in opposite directions.

To perform the interfacial smoothing, we first average the position $\boldsymbol{x}$ of the edge points across neighbor elements, e.g.,

$$\boldsymbol{x}_a^{\text{new}} = \boldsymbol{x}_b^{\text{new}} = \frac{(\boldsymbol{x}_a^{\text{old}} + \boldsymbol{x}_b^{\text{old}})}{2}. \tag{12}$$

(Note that the smoothing above involves more than two points at the element vertices.) We then calculate the geometric properties of the updated shape $\boldsymbol{x}^{\text{new}}$. In this way the interface is continuous along the local tangent direction parallel to the element edges; for our specific example the derivatives $(\partial \boldsymbol{x}/\partial\eta)_a$ and $(\partial \boldsymbol{x}/\partial\xi)_b$ are identical.

The next step is to achieve continuity in the local tangent direction normal to the element edges. For this, we calculate the unit tangent vectors along this local direction, e.g.,

$$(\boldsymbol{t}_1^L)_a = \frac{\left(\frac{\partial \boldsymbol{x}}{\partial \eta}\right)_a \times \boldsymbol{v}_a}{\left|\left(\frac{\partial \boldsymbol{x}}{\partial \eta}\right)_a \times \boldsymbol{v}_a\right|}, \tag{13}$$

where $\boldsymbol{v}_a$ is the nonunit normal vector at point a, $\boldsymbol{v}_a = (\partial \boldsymbol{x}/\partial\xi)_a \times (\partial \boldsymbol{x}/\partial\eta)_a$. [The unit tangent $(\boldsymbol{t}_2^L)_b$ is determined in a similar way.] Note that the tangent vectors $(\boldsymbol{t}_1^L)_a$ and $(\boldsymbol{t}_2^L)_b$ lie along the x_1^L axis at the point a and the x_2^L axis at the point b, respectively. In order to achieve continuity in this tangent direction, we average the unit tangent vectors, e.g.,

$$(\boldsymbol{t}_1^L)_a^{\text{new}} = -(\boldsymbol{t}_2^L)_b^{\text{new}} = \frac{(\boldsymbol{t}_1^L)_a^{\text{old}} - (\boldsymbol{t}_2^L)_b^{\text{old}}}{2}, \tag{14}$$

where the minus sign appears due to the specific geometry shown in Fig. 4. The tangent vectors $(\boldsymbol{t}_1^L)_a^{\text{new}}$ and $(\boldsymbol{t}_2^L)_b^{\text{new}}$ are then normalized.

At this point, both the position and the tangent vectors at the edge points are continuous across the elements. The next step is to determine the updated first derivatives $(\partial \boldsymbol{x}/\partial\xi)_a^{\text{new}}$ and $(\partial \boldsymbol{x}/\partial\eta)_b^{\text{new}}$. From the tangent vectors, we calculate the unit normal vectors, e.g.,

$$\boldsymbol{n}_a^{\text{new}} = \frac{(\boldsymbol{t}_1^L)_a^{\text{new}} \times \left(\frac{\partial \boldsymbol{x}}{\partial \eta}\right)_a}{\left|(\boldsymbol{t}_1^L)_a^{\text{new}} \times \left(\frac{\partial \boldsymbol{x}}{\partial \eta}\right)_a\right|}. \tag{15}$$

Note that $\boldsymbol{n}_a^{\text{new}}$ and $\boldsymbol{n}_b^{\text{new}}$ are identical now due to the interfacial smoothing we have performed. To determine the updated derivative $(\partial \boldsymbol{x}/\partial\xi)_a^{\text{new}}$, the following relations at the point a are applied:

$$\boldsymbol{n}_a^{\text{new}} \cdot \left(\frac{\partial \boldsymbol{x}}{\partial \xi}\right)_a^{\text{new}} = 0, \tag{16}$$

$$\left(\frac{\partial \boldsymbol{x}}{\partial \xi}\right)_a^{\text{new}} \cdot \left(\frac{\partial \boldsymbol{x}}{\partial \eta}\right)_a = \left(\frac{\partial \boldsymbol{x}}{\partial \xi}\right)_a^{\text{old}} \cdot \left(\frac{\partial \boldsymbol{x}}{\partial \eta}\right)_a, \tag{17}$$

$$\left|\left(\frac{\partial \boldsymbol{x}}{\partial \xi}\right)_a^{\text{new}}\right| = \left|\left(\frac{\partial \boldsymbol{x}}{\partial \xi}\right)_a^{\text{old}}\right|. \tag{18}$$

The smoothed derivative $(\partial \boldsymbol{x}/\partial\eta)_b^{\text{new}}$ is determined in a similar way.

So far, we have smoothed the position $\boldsymbol{x}$ and the first derivatives, $(\partial \boldsymbol{x}/\partial\xi)$ and $(\partial \boldsymbol{x}/\partial\eta)$, at the edge points across the spectral elements. We want to employ this updated information at the edge points to derive a smoothed interfacial shape. To achieve this goal, we have developed a suitable two-dimensional Hermitian interpolation that utilizes the function and first derivative values at the end points, but only function values at the interior points. This interpolation involves two nested one-dimensional Hermitian interpolations developed in Ref. 30 for the deformation of two-dimensional droplets,

$$\begin{aligned} f(x) = {} & (x^2-1)^2 \sum_{i=1}^{M} \frac{1}{(x_i^2-1)^2} \prod_{j\neq i}^{M} \left(\frac{x-x_j}{x_i-x_j}\right) f(x_i) \\ & + \prod_{j=1}^{M} \left(\frac{x-x_j}{-1-x_j}\right) \frac{(x-1)^2}{4}(x+1) f'(-1) \\ & + \prod_{j=1}^{M} \left(\frac{x-x_j}{1-x_j}\right) \frac{(x+1)^2}{4}(x-1) f'(+1) \\ & + \prod_{j=1}^{M} \left(\frac{x-x_j}{-1-x_j}\right) \frac{(x-1)^2}{4}[1+b_{(-1)}(x+1)] f(-1) \\ & + \prod_{j=1}^{M} \left(\frac{x-x_j}{1-x_j}\right) \frac{(x+1)^2}{4}[1-b_{(+1)}(x-1)] f(+1). \end{aligned} \tag{19}$$

The function values $f(\pm 1)$ and the first derivatives $f'(\pm 1)$ correspond to the smoothed position $\boldsymbol{x}$ and the updated $(\partial \boldsymbol{x}/\partial\xi)$ or $(\partial \boldsymbol{x}/\partial\eta)$ of the edge points, respectively. The coefficients $b_{(-1)}$ and $b_{(+1)}$ are chosen to yield zero slope at the element edges,

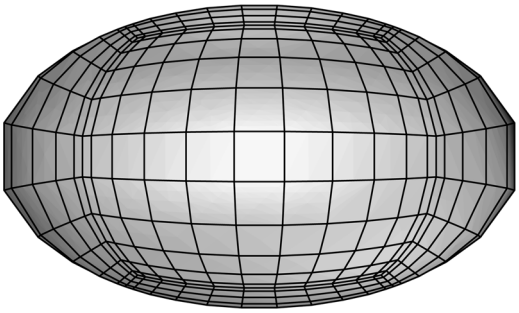

FIG. 5. Time evolution of a droplet in a planar extensional flow for the same parameters as in Fig. 3, except that now our first-order interfacial smoothing is employed after each time step. The droplet shape is shown for time $t=0.28$, i.e., step $N_{\text{step}}=140$. The drop interface is continuous and smooth across the spectral elements at all times.

$$b_{(-1)} = -\left[\sum_{j=1}^{M}\left(\frac{1}{x-x_j}\right)+\frac{2}{x-1}\right]_{x=-1} = \sum_{j=1}^{M}\left(\frac{1}{1+x_j}\right)+1, \tag{20}$$

$$b_{(+1)} = +\left[\sum_{j=1}^{M}\left(\frac{1}{x-x_j}\right)+\frac{2}{x+1}\right]_{x=+1} = \sum_{j=1}^{M}\left(\frac{1}{1-x_j}\right)+1. \tag{21}$$

To preserve the degrees of freedom of our Gauss-Lobatto discretization, on each spectral element we determine $(N_B-4)\times(N_B-4)$ interior Jacobi points along each curvilinear coordinate from the existing $N_B\times N_B$ Lobatto points by typical Lagrangian interpolation. We emphasize that for each curvilinear direction, the position and the first derivative at the two end points count for the missing four degrees of freedom. By combining these interior Jacobi points with the smoothed position $\boldsymbol{x}$ and the first derivatives $(\partial\boldsymbol{x}/\partial\xi)$ and $(\partial\boldsymbol{x}/\partial\eta)$ at the edge points, the two-dimensional Hermitian interpolation based on Eq. (19) is employed on each spectral element (with $M=N_B-4$) to produce a new set of $N_B\times N_B$ Gauss-Lobatto points that represents the final smoothed interfacial shape at time $t+\Delta t$.

In Fig. 5 we show the time evolution of the droplet presented earlier in Fig. 3, but now we employ our first-order smoothing scheme after each time step. In contrast to Fig. 3, the drop interface is now continuous and smooth across the spectral elements at all times.

We emphasize that by employing our first-order smoothing scheme, we formally achieve continuity of the position and the tangent/normal vectors at the edges of the spectral elements. However, for the problems we have studied so far, at both subcritical and supercritical capillary numbers (i.e., at both small and large deformations), our numerical results reveal that this technique also achieves continuity of the curvature at the element edges, i.e., continuity of the second derivative of the interfacial geometry. This seems to contradict the experience based on low-order interpolation algorithms, where to achieve continuity of the interfacial curvature, one may need to employ an interpolation that formally preserves the continuity of both first and second derivatives of the interfacial shape (e.g., spline interpolation). The difference lies on the fact that in our case, each spectral element covers a large portion of the interfacial area, where the spectral interpolation produces a smooth distribution of high derivatives of the interfacial geometry. In this case, by smoothing only the position and its first derivative at the element edges, we also achieve smoothing of higher derivatives of the interfacial shape.

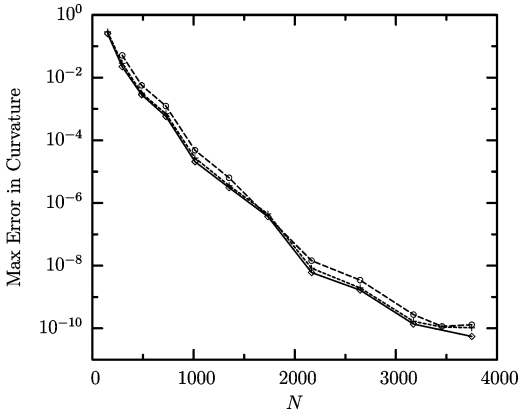

FIG. 6. The maximum absolute error in the computed curvature versus the number of spectral points $N=N_EN_B^2$ for different spheroids: —, $a=b=c=1$; ----, $a=b=1$, $c=0.4$; – – –, $a=1$, $b=c=0.4$. The exponential convergence shown in this figure was generated by employing $N_E=6$ spectral elements and varying the number of basis points N_B from 5 to 25. The exact value was used to determine the numerical error.

As a closure to this section, we emphasize that the smoothing methodology we have developed is an efficient technique to preserve the continuity of the interfacial spectral geometry and its derivatives. The entire process, including the relevant two-dimensional Hermitian interpolation, requires a computational cost of only $O(N_EN_B)$, i.e., $O(N_B)$ on each spectral element, owing to the fact that it is implemented through products of one-dimensional rules. (The reduction of the operation cost is a characteristic feature of all product rules in spectral methods.[11]) Since in these interpolations we employ high-order orthogonal polynomials, the loss of accuracy from one to the other discretization is negligible. In addition, by implementing the smoothing scheme *after* we determine the (temporary) interfacial shape at the desired time $t+\Delta t$, we have the advantage of avoiding incorporating a smoothing technique (e.g., the Hermitian interpolation) inside the spectral element algorithm for the solution of the corresponding boundary integral equation. Most importantly, our smoothing methodology preserves the main characteristic of the spectral methods, i.e., the exponential convergence in the interfacial accuracy with increasing the number of spectral points, as discussed in Sec. V A.

V. PROPERTIES OF INTERFACIAL ALGORITHM

A. Convergence: Curvature and deformation

The exponential convergence in the numerical accuracy with increasing the number of spectral points, $N=N_EN_B^2$, is evident both for the geometric properties of a given shape, such as the interfacial curvature, as well as for the dynamic evolution of the interfacial shape. Figure 6 shows the maximum absolute error in the computed curvature as the number

of spectral points N increases from 150 to 3750 for different spheroidal droplets. The exponential convergence of our spectral algorithm is in direct contrast to the common linear or quadratic convergence associated with low-order algorithms. For example, Loewenberg and Hinch[8] reported a pointwise accuracy in curvature of $O(N^{-1/2})$ and a $O(N^{-1})$ accuracy in the integrals of curvature over a large portion of the interfacial shape. Zinchenko, Rother, and Davis[9] in their Fig. 5(b) reported a linear convergence by increasing the number of the employed triangles N_t and an error $\approx 4\times 10^{-2}$ for $N_t=5120$. (Note that our algorithm shows an error $\approx 1\times 10^{-10}$ for $N=3456$.) The same accuracy should characterize the algorithm of Cristini, Blawzdziewicz, and Loewenberg[27] since they employ a similar method for the calculation of the curvature and normal vectors. Bazhlekov, Anderson, and Meijer[10] reported an error of 14% independent of discretization for the computed curvature of an analytically given spherical shape. They also reported a quadratic convergence if the spherical droplet was let to relax in the absence of any external forcing; in this case in their Fig. 4 an error $\approx 1.5\times 10^{-4}$ was shown for $N_t=10\,000$ triangles.

The exponential convergence in the numerical accuracy is also evident for the dynamic evolution of the interfacial shape. To determine the droplet deformation with time, we monitor the droplet's longest and shortest semiaxes, L and S, respectively, as well as Taylor's deformation parameter

$$D=\frac{L-S}{L+S}. \tag{22}$$

These semiaxes are determined as the maximum and minimum distance from the droplet's centroid to the interface by employing a Newton method for the optimization problems. We also calculate L, S, and D by the semiaxes of the ellipsoid that has the same inertia tensor as the droplet; this way we also monitor the evolution of the third dimension of the droplet, i.e., its depth W.

Figure 7 shows the exponential convergence in the numerical accuracy of calculating the interfacial shape for a droplet with $\lambda=0.5$ in a planar extensional flow at subcritical and supercritical conditions. We consider two cases: motion of the interfacial spectral points along only the normal velocity as well as utilization of a tangential velocity $U_t\boldsymbol{t}$. In both cases, our algorithm shows the typical exponential convergence of the spectral methods with increasing number of spectral points N. Moreover, the utilization of a tangential velocity $U_t\boldsymbol{t}$ produces a more uniform distribution of the spectral points and thus it improves the accuracy up to almost two orders of magnitude. We emphasize that the difference in the interfacial accuracy between our spectral algorithm and low-order methods is dramatic since the latter commonly achieve linear convergence by increasing the number of the employed grid points.[26,27]

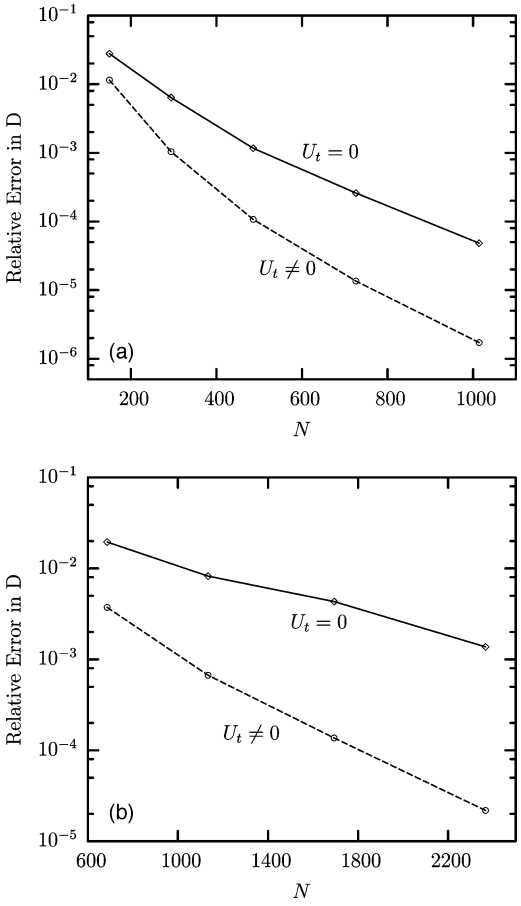

FIG. 7. The relative error in the computed deformation D versus the number of spectral points $N=N_E N_B^2$ for a droplet with $\lambda=0.5$ in a planar extensional flow. (a) Subcritical flow with Ca=0.13 at time $t=0.3$. (Note that $D=0.205$ while the droplet length has been increased by 24% while its width has been decreased by 18%.) The exponential convergence shown was generated by employing $N_E=6$ spectral elements and varying the number of basis points N_B from 7 to 13. (b) Supercritical flow with Ca=0.25 at time $t=1$. (Note that $D=0.523$ while the droplet length has been increased by 91% and its width has been decreased by 40%.) The exponential convergence shown was generated by employing $N_E=14$ spectral elements and varying the number of basis points N_B from 7 to 13. In both cases, the results for $N_B=15$ were used to determine the numerical error. We employed the interfacial tangential velocity $U_t\boldsymbol{t}=c_t[(\boldsymbol{u}\cdot\boldsymbol{t}_1)\boldsymbol{t}_1+(\boldsymbol{u}\cdot\boldsymbol{t}_2)\boldsymbol{t}_2]$, with $c_t=0.5$ in (a) and $c_t=1.5D$ in (b), where $\boldsymbol{t}_1$ and $\boldsymbol{t}_2$ are the two unit tangent vectors on the droplet interface.

B. Adaptive mesh reconstruction

In strong flows, especially those corresponding to supercritical conditions, the droplet may elongate significantly; thus the original spectral discretization $\{N_E,N_B\}$ may not be sufficient to describe a very deformed interfacial shape. To resolve this issue, one may change one or both of the discretization parameters of the spectral boundary elements, i.e., N_E and N_B. In the current implementation of our algorithm, it is more efficient to change only the number of elements. Since the spectral elements we employ are quadrilateral, two distinct cases may be found.

In the first case, the relevant length of a spectral element is increased above a prescribed maximum limit along only one curvilinear direction. In such a case the element is divided into two halves, with $N_B\times N_B$ basis points, as shown in Fig. 8(a). This case may represent the development of an interfacial neck. In the second case, the relevant length of a spectral element along both curvilinear directions is increased above a prescribed maximum limit. In such a case the element should be divided in both directions; our preference is to divide the element into five elements, as shown in

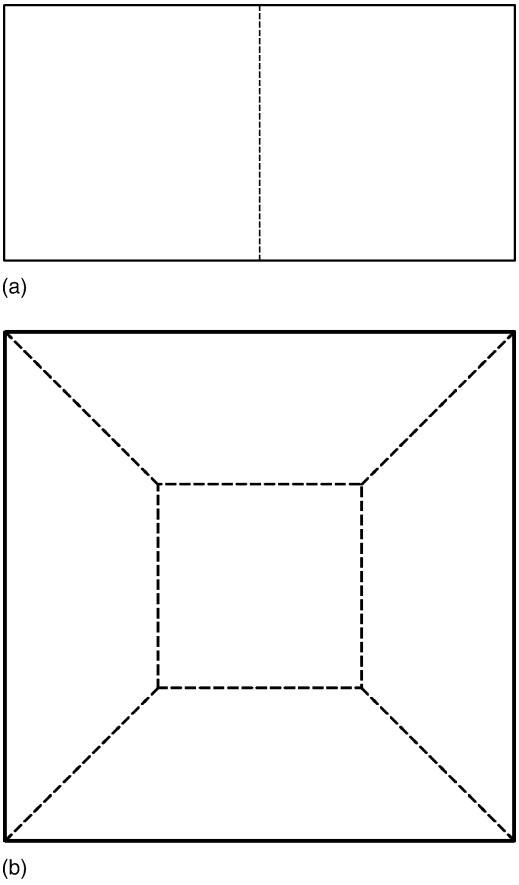

FIG. 8. Layout for element division into (a) two and (b) five elements. The solid line represents the original element while the dashed lines show the resulting elements after division.

Fig. 8(b). This case may represent the two edges of an elongated droplet that show large interfacial curvature. For each case, the opposite occurs when the relevant length of a spectral element is decreased below a prescribed minimum limit; in this case the element is combined with its neighbor(s) while $N_B \times N_B$ new basis points are defined on the resulting element. The employed time step Δt is accordingly adjusted to satisfy the Courant condition, Eq. (11).

The goal of our adaptive mesh reconstruction is to produce a reasonable spectral element discretization of the interfacial shape with respect to the element's arclengths and/or the variation of curvature on it. Thus, as relevant lengths of a spectral element are regarded, its arclength L_1 and its curvature length L_2 along each curvilinear direction,

$$L_1 = \int_{\text{elem}} \mathrm{d}\ell, \quad L_2 = R_{\text{ref}} \int_{\text{elem}} |\boldsymbol{\nabla} \cdot \boldsymbol{n}| \mathrm{d}\ell, \tag{23}$$

where $\mathrm{d}\ell$ is the arclength and R_{ref}, some reference radius of curvature. For problems involving surfaces in close contact, another relevant length can be considered associated with the surfaces' gap.[27] Thus, our adaptive mesh procedure is similar to the ones employed in low-order algorithms, e.g., Refs. 27 and 31. Note that our procedure is based on the size of the spectral elements, and not of successive grid points; thus it requires a smaller number of comparisons and decision making operations (i.e., divide, unite, or no change).

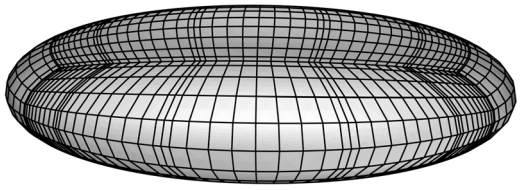

FIG. 9. Example of element division: droplet shape for $\lambda=0.5$ and $\mathrm{Ca}=0.25$ at time $t=1$ in a planar extensional flow. The droplet deformation is $D=0.52$, its length L has been increased by 91% while its width has been decreased by 40%. The original spherical shape is divided into $N_E=6$ spectral elements with $N_B=11$ basis points similar to that shown in Fig. 1. As the droplet deformation increases, the number of spectral elements is increased by employing element division into five new elements at the two edges of the droplet. The shape shown with $N_E=22$ results after two such divisions.

This strategy has been employed to determine large deformations of droplets in supercritical conditions. Figure 9 shows the interfacial shape of a droplet with $\lambda=0.5$ for $\mathrm{Ca}=0.25$ in a planar extensional flow. (For this system, the critical flow rate is $\mathrm{Ca}\approx 0.135$ based on our numerical results and the experimental findings of Ref. 32.) Note that the initial spherical shape is discretized into $N_E=6$ spectral elements, as shown in Fig. 1. As the drop deformation increases, more elements are employed by division of each of the two edges of the droplet into five new elements; the current shape results after two such divisions.

C. Comparisons with previous studies

We have conducted numerous tests to verify the reliability and robustness of our algorithm involving free-suspended droplets and bubbles under flow and/or gravity conditions. For example, our computational results for the transient evolution in simple shear flow show very good agreement with the experimental findings reported in Figs. 5 and 6 of Ref. 33, and are in excellent agreement with the corresponding computations by Pozrikidis included in Ref. 33. In addition, our computations are in excellent agreement with the numerical results for the transient evolution of a droplet in a planar extensional flow reported in Fig. 8 of Ref. 10. Our predictions for the equilibrium droplet shape are in excellent agreement with the analytical predictions of Taylor[34] as well as with those resulted by our Newton method for the direct calculation of equilibrium shapes under steady flow conditions.[19] More comparisons may be found in Ref. 35.

We proceed with additional comparisons with the experimental results of Bentley and Leal[32], who studied the droplet deformation in planar four-roll mill flows $\boldsymbol{u}^{\infty}=(u_x,u_y,0)$ with

$$u_x = \frac{G}{2}[(1+a_f)x + (1-a_f)y],$$
$$u_y = \frac{G}{2}[(-1+a_f)x - (1+a_f)y]. \tag{24}$$

In particular, in Fig. 10 we present the evolution of a droplet with $\lambda=0.118$ in the flow defined by $a_f=0.6$. The time evolution of the droplet deformation D is shown in Fig. 10(a) for three capillary numbers used in the experimental study (see Fig. 9 in Ref. 32). The corresponding equilibrium values,

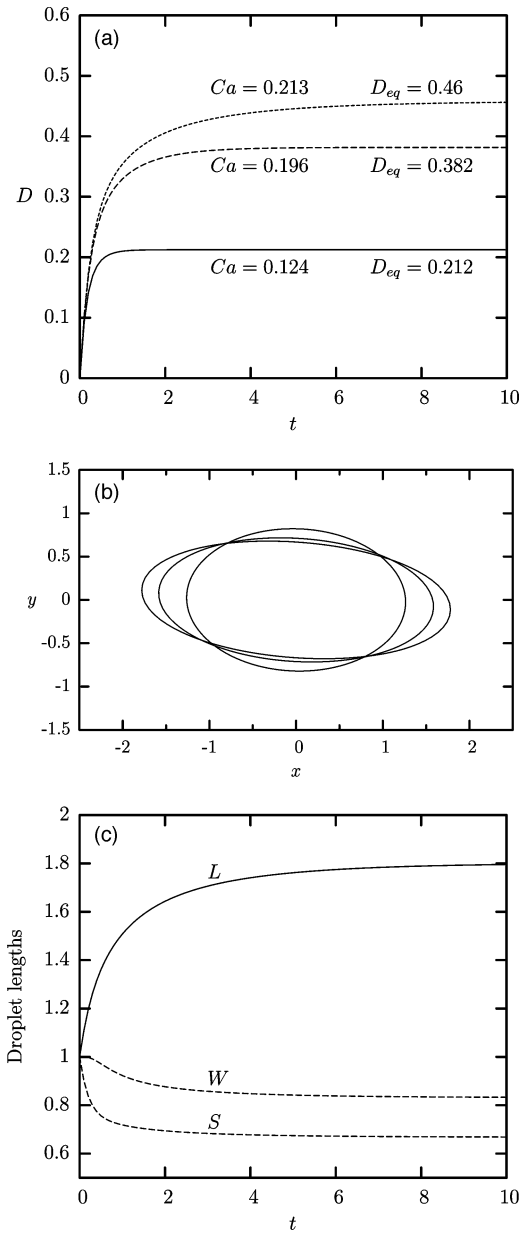

FIG. 10. Subcritical evolution of a droplet with $\lambda=0.118$ in a planar four-roll mill flow with $a_f=0.6$. (a) Time evolution of the droplet deformation D for Ca=0.124,0.196,0.213. (Note that for Ca=0.213 our computations cover the time period [0,20] even though we present results only in [0,10].) (b) Droplet profiles at equilibrium for Ca=0.124,0.196,0.213. (c) Time evolution of the droplet's length L, width S, and depth W for Ca=0.213. Our results for the equilibrium deformation D_{eq} and drop profile are in excellent agreement with the experimental findings of Bentley and Leal (Ref. 32) reported in their Fig. 9.

$D_{\text{eq}}=0.212,0.382,0.46$, are in excellent agreement with the experimental findings, i.e., $D_{\text{eq}}^{BL}=0.211,0.381,0.479$. Note that our results for Ca=0.213 have been verified with different numerical grids and thus we believe that they are accurate as presented. The droplet profiles at equilibrium shown in Fig. 10(b) are also in excellent agreement with the experimental results. Finally, in Fig. 10(c) we present the evolution of the droplet's length L, width S and depth W for capillary number $Ca=0.213$.

We consider now the dynamics near the critical conditions, i.e., near the flow rate at which equilibrium interfacial shapes cease to exist. Figure 11 shows the evolution of the deformation D for a droplet with viscosity ratio $\lambda=0.2$ in a planar extensional flow (i.e., a four-roll mill flow with $a_f=0$). The critical capillary number (i.e., $\text{Ca}\approx 0.155$) is in excellent agreement with experimental findings.[32]

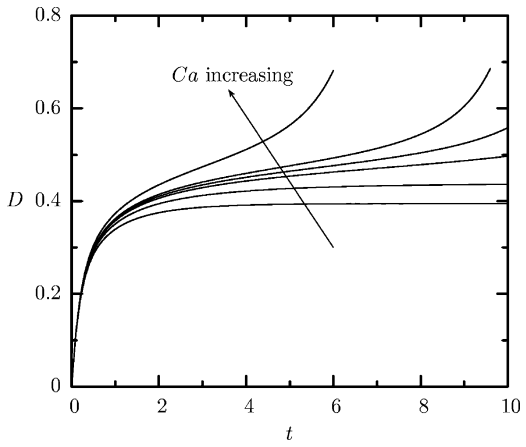

FIG. 11. Dynamics near the critical point for a droplet with viscosity ratio $\lambda=0.2$ in a planar extensional flow: droplet deformation D versus time t. The capillary number is Ca=0.15,0.155,0.158,0.159,0.16,0.165.

The time evolution of the major semiaxis L of a droplet with viscosity ratio $\lambda=0.2$ in a planar extensional flow under supercritical conditions (i.e., Ca=0.16) is shown in Fig. 12. In addition, the drop profiles at several times are included in the figure's inset. Initially the drop is discretized into $N_E=6$ spectral elements; as the drop deformation increases, more elements are employed by division of each of the two edges of the droplet into five new elements. At time $t=12.5$, three such divisions have been made, resulting in a total of $N_E=30$ spectral elements. We emphasize that our results are in excellent qualitative agreement with the experimental findings of Ha and Leal[36] reported in their Fig. 2.

As a closure, we emphasize that in this section we have presented the basic properties of our interfacial spectral al-

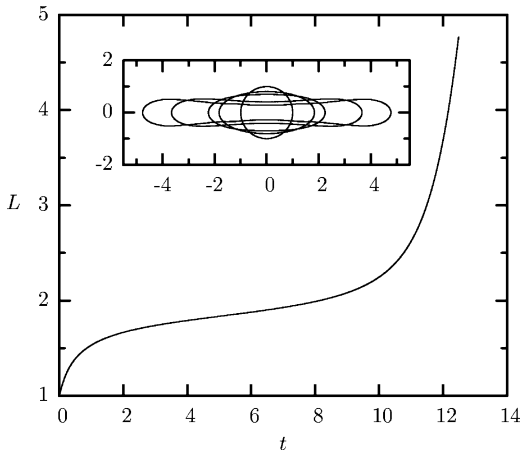

FIG. 12. Supercritical evolution of a droplet with viscosity ratio $\lambda=0.2$ in a planar extensional flow with Ca=0.16: time evolution of the droplet's major semiaxis L. The inset shows the drop profile (i.e., the drop intersection with the plane $z=0$) at times $t=0,5,10,12,12.5$. Our results are in excellent agreement with the experimental findings of Ha and Leal (Ref. 36) reported in their Fig. 2.

gorithm, including its exponential convergence in numerical accuracy and the associated adaptive mesh reconstruction procedure, by focusing on interfacial deformation of free-suspended droplets in several types of flows. However, our interfacial spectral algorithm is not restricted to those problems only. For example, the excellent performance of the spectral method for surfaces in close contact has been well demonstrated in Muldowney and Higdon.[15] Additional physical problems (e.g., interfaces in close contact or in narrow microfluidic channels) will be presented in future publications.

VI. MOTION OF A BUOYANT DROP NEAR A VERTICAL WALL

The motion of solid particles and deformable droplets and bubbles near solid surfaces in external flow conditions or gravity has received much attention during the last decades. Several studies have considered the drag, rising, and migration motion of solid particles in constrained geometries at both low and finite Reynolds numbers, e.g., Refs. 37–42. Efforts have also been made to understand the rising and migration motion of deformable droplets and bubbles near solid walls in shear and Poiseuille flows or under gravity, e.g., Refs. 23 and 43–50. Chan and Leal[43] solved analytically the motion of a droplet in simple shear and Poiseuille flows for Newtonian and non-Newtonian surrounding fluids. Shapire and Haber studied analytically the motion of a droplet in a quiescent fluid between two parallel plates,[44] as well as the droplet motion in shear flow in the presence of solid walls.[45] Experimental studies considered the motion of droplets and bubbles near solid walls, e.g., Refs. 46 and 49. Computational studies compared their results with analytical predictions for the droplet motion in a linear shear flow near a plane wall;[47,48] these comparisons reveal that analytical models overestimate the droplet migration velocity. Hudson[51] studied the wall migration and shear-induced diffusion of fluid droplets in emulsions. An extended review on the motion of particles and droplets near solid surfaces may be found in the recent work of Magnaudet, Takagi, and Legendre.[23]

In this section, we focus our interest in understanding the inertialess motion of a buoyant droplet left from an initial spherical shape close to a vertical wall. This problem has been included in the recent study of Magnaudet, Takagi, and Legendre,[23] who considered the effects of deformation, inertia, and linear shear flow on the motion of a buoyant droplet near a solid wall. We emphasize that the aforementioned analytical investigation[23] is based on quasisteady conditions, i.e., the time plays no direct role in the droplet motion. In addition, the analytical predictions for the lateral droplet migration are formally valid for $\lambda B_d \ll 1$, but are expected to be practically valid for $\lambda B_d \leqslant 1$. (See Sec. 3.2 in Ref. 23.)

Thus, our goal in this study is to investigate the (initial) transient effects on the droplet motion while we also compare our numerical results with the analytical predictions[23] to verify their range of validity. Of particular importance is the verification (or rejection) of the analytical prediction that the direction of lateral migration depends on the viscosity ratio.[23] We note that due to the interfacial deformation, a rising droplet near a solid wall experiences a lateral migration, even under Stokes flow conditions.[23,40]

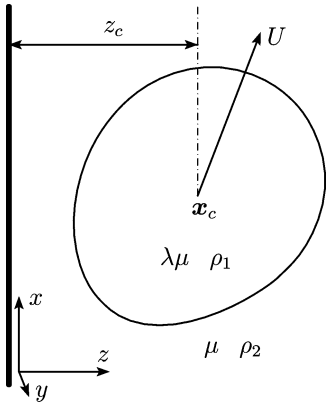

FIG. 13. Illustration of a buoyant droplet moving near a vertical solid wall.

Figure 13 illustrates the motion of a fluid droplet (fluid 1) with density ρ_1 and viscosity $\lambda\mu$ in an otherwise quiescent viscous fluid (fluid 2) with density ρ_2 and viscosity μ near a stationary vertical solid wall. The gravitational acceleration is g while the surface tension γ is assumed constant. The volume centroid of the droplet is denoted as $\boldsymbol{x}_c$ while z_{c0} is the initial distance from the wall where the spherical drop is left to rise.

The characteristic length a of the droplet is used as the length scale while the time is scaled with the buoyancy time scale $\tau_g = \mu/\Delta\rho\, ga$ (where $\Delta\rho = |\rho_2 - \rho_1|$), and thus the velocity scale of rising is $U = \Delta\rho\, ga^2/\mu$. The droplet motion and shape is affected by the Bond number, defined previously in Eq. (1), which represents the ratio of gravitational forces to interfacial forces. For convenience, we assume that the density of the droplet is smaller than that of the surrounding fluid, and thus the droplet rises. However, our study also represents a heavier droplet sedimenting in an otherwise quiescent fluid. In this study we consider that the inertia effects on the drop dynamics are negligible, i.e., the Grashof number is very small, $\sqrt{G_r} = \rho_2 Ua/\mu = \rho_2\, \Delta\rho\, ga^3/\mu^2 \ll 1$. Thus our study is commonly valid for highly viscous liquids.

The governing equations, Stokes and continuity, along with the boundary conditions at the droplet interface were given in Sec. II. In addition, $\boldsymbol{u} = 0$ on the solid wall. The velocity at a point $\boldsymbol{x}_0$ on the droplet interface S_d or on the solid wall S_w satisfies the following boundary integral equation:

$$\Omega \boldsymbol{u}(\boldsymbol{x}_0) - 4\pi\mu \boldsymbol{u}^{\infty}(\boldsymbol{x}_0) = -\int_{S_d} \{\boldsymbol{S}\cdot(\Delta\boldsymbol{f} - \boldsymbol{f}^{\infty}) - \mu \boldsymbol{T}\cdot[(1-\lambda)\boldsymbol{u} - \boldsymbol{u}^{\infty}]\cdot\boldsymbol{n}\} dS - \int_{S_w} [\boldsymbol{S}\cdot(\boldsymbol{f}_2 - \boldsymbol{f}^{\infty}) - \mu \boldsymbol{T}\cdot(\boldsymbol{u}_2 - \boldsymbol{u}^{\infty})\cdot\boldsymbol{n}] dS, \quad (25)$$

where the coefficient Ω takes values $4\pi\mu(1+\lambda)$ and $4\pi\mu$ for points $\boldsymbol{x}_0$ on the surfaces S_d and S_w, respectively. The fundamental solution of the three-dimensional Stokes equations, $\boldsymbol{S}$ and $\boldsymbol{T}$, are given by Eq. (7). For the specific problem studied

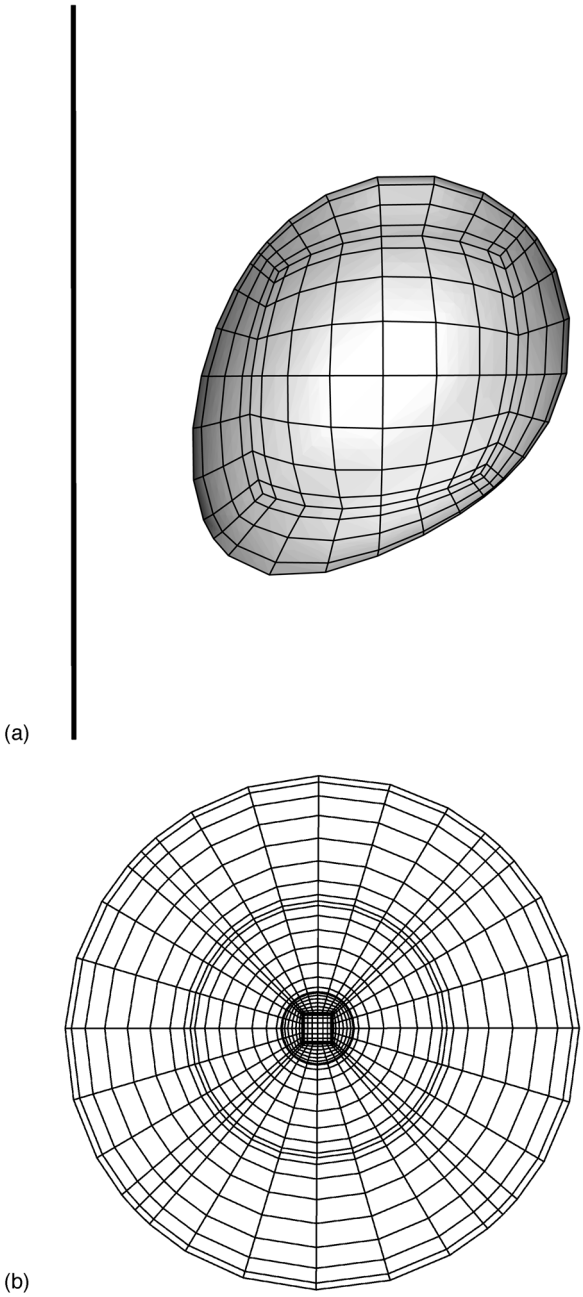

FIG. 14. Discretization of geometry for spectral boundary element calculation in the case of a droplet moving near a vertical wall: (a) droplet interface and (b) solid wall. The interfacial shape shown corresponds to a droplet with $B_d=3$ and $\lambda=1$ at an initial distance from the wall $z_{c0}=1.5$ and at time $t=20$, where $z_c\approx 1.61$.

here, the undisturbed velocity and force are $\boldsymbol{u}^\infty=\boldsymbol{f}^\infty=0$.

The initial droplet interface is discretized into six equal-size spectral elements while the solid surface is discretized into a central square element with three or four rows of four elements around it, as shown in Fig. 14. In our computations, the radius of the solid surface (which formally should extend to infinity) is at least 14 times the characteristic drop radius a; this creates negligible error in all cases.

Due to the translation of the droplet, the discretized solid wall follows the droplet rising, i.e., the center of the square element shown in Fig. 14(b) is defined with respect to the droplet centroid. To avoid severe grid distortion on the droplet interface due to the drop's translation, in the time evolution of the interface given by Eq. (10) we employ the tangential velocity

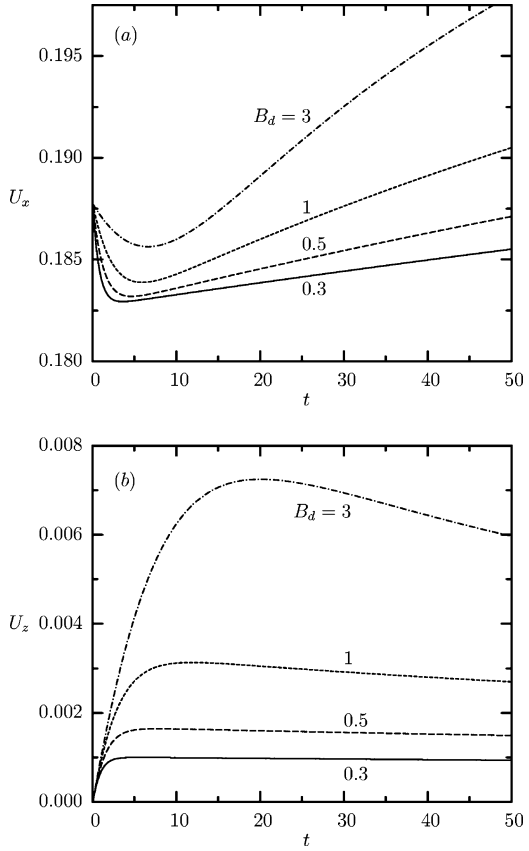

FIG. 15. Time evolution of the velocity of a droplet with $\lambda=1$ for Bond number $B_d=0.3,0.5,1,3$: (a) rising velocity U_x and (b) migration velocity U_z. The initial drop lateral location is $z_{c0}=1.5$.

$$U_t=c_t(\boldsymbol{u}\cdot\boldsymbol{t})+(1-c_t)(\boldsymbol{u}_c\cdot\boldsymbol{t}), \tag{26}$$

where $\boldsymbol{u}_c$ is the droplet's translational velocity (i.e., the velocity of the drop centroid) while in most of the runs we employed $c_t=0$. In essence, the kinematic condition at the interface, employed via Eqs. (10) and (26), shows that in this case the droplet grid is first translated by the droplet translational velocity and then deformed (with respect to its new center of mass) in a manner similar to that described earlier for free-suspended droplets with a fixed center of mass.

The velocity of the buoyant droplet with $\lambda=1$ placed at an initial distance $z_{c0}=1.5$ from a vertical wall is shown in Fig. 15. The drop rising velocity U_x first decreases and then shows a steady increase toward its highest value, i.e., that for rising in an unbounded fluid that in dimensionless form is $U_x^\infty=2(1+\lambda)/(6+9\lambda)$.[23,52] The rising velocity is a monotonic function of the Bond number B_d; this is a direct result of the presence of the solid wall since in the absence of the solid wall the rising velocity does not depend on B_d. On the other hand, the droplet migration velocity U_z shows an initial fast increase, followed by a slow decrease toward its zero value far from the wall. Note that in Fig. 15(b) the curves for $B_d\leqslant 1$ do not show a plateau for U_z but a very slow decrease over time. The migration velocity is larger for higher Bond

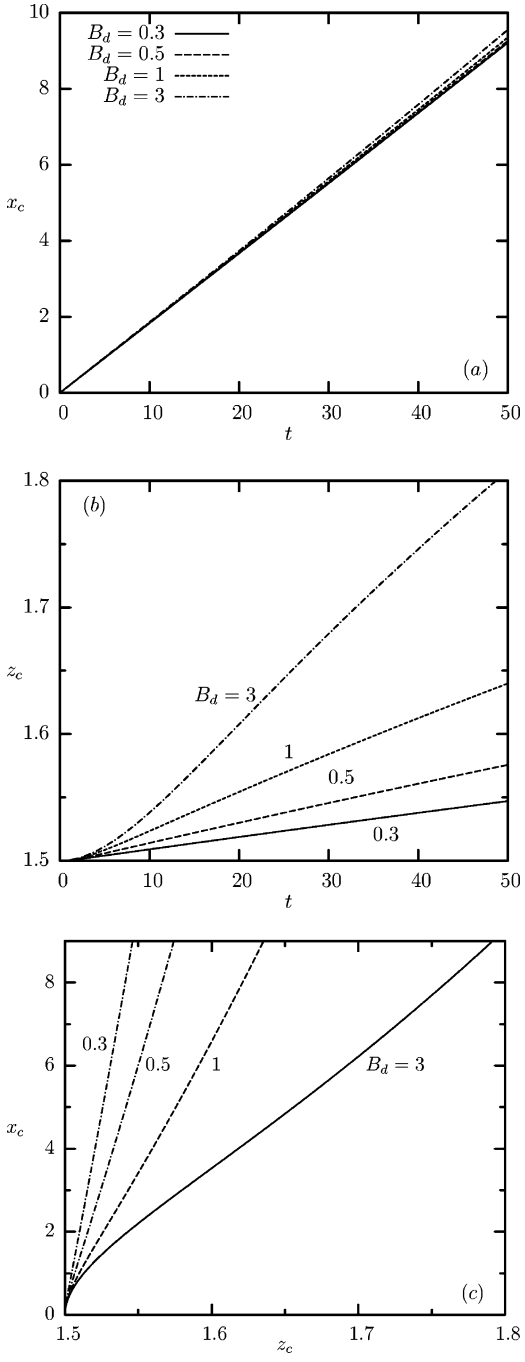

FIG. 16. Evolution of the position of a droplet with $\lambda=1$ for Bond number $B_d=0.3,0.5,1,3$. (a) Time evolution of the centroid coordinate x_c. (b) The same as in (a) but for z_c. (c) Rising x_c versus lateral migration z_c. The initial drop location is $(x_{c0},z_{c0})=(0,1.5)$.

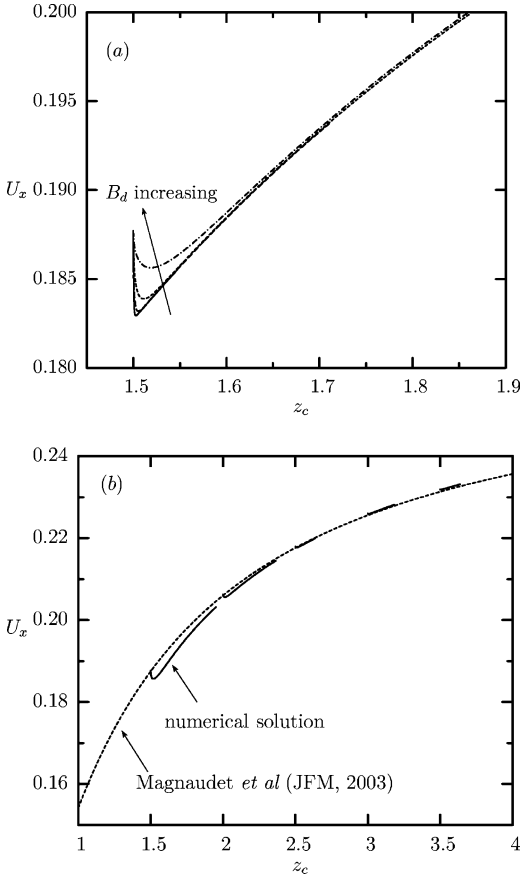

FIG. 17. Rising velocity U_x of a droplet with $\lambda=1$ versus its lateral position z_c. (a) The initial drop location is $z_{c0}=1.5$ while $B_d=0.3,0.5,1,3$. (b) The Bond number is $B_d=3$ while the initial drop location is $z_{c0}=1.5,2,2.5,3,3.5$. Also included is the rising velocity of a spherical droplet (----) at a distance z_c from the wall found in Ref. 23.

number B_d; this results from both the increased rising velocity U_x as well as the increased interfacial deformation with B_d shown later in Figs. 19(a) and 20.

Comparing the magnitude of U_x and U_z, one readily realizes that the droplet's migration motion away from the wall is much slower than its rising motion, especially for a small Bond number. This is shown clearly in Fig. 16, where we plot the coordinates of the drop centroid. Note that the Bond number has rather negligible effects on the vertical position of the droplet, but it affects greatly the drop lateral position, as shown in Figs. 16(a) and 16(b). Thus, for the same initial location, the less buoyant drop shows more rising than lateral migration, as also shown in Fig. 16(c), where we plot the vertical coordinate x_c of the drop versus its lateral location z_c.

We now focus on the vertical motion of the droplet with respect to the droplet's lateral position. As Fig. 17(a) reveals, the Bond number B_d affects the rising velocity U_x slightly, and only close to the wall; as the drop migrates away from the solid, its rising velocity becomes independent of the Bond number. Thus, in Fig. 17(b) we plot U_x vs z_c for the same Bond number, for droplets with different initial positions from the wall, i.e., $z_{c0}=1.5,2,2.5,3,3.5$. As the drop migrates away from the wall, the effects of the droplet deformation on the rising velocity is expected to become weak and after some distance negligible. To show this, in Fig. 17(b) we also include the rising velocity of a spherical droplet based on the zeroth-order analysis found in the recent study of Magnaudet, Takagi, and Legendre.[23] [See Eqs. (12) and (3b) in the analytical study;[23] we have verified this velocity computationally by placing a spherical droplet at increasing distances from the wall.] Comparing our results for the actual rising velocity U_x of (deformed) droplets with that from the spherical approximation, we see that only close to the wall and for a high Bond number, the actual U_x shows a variation from its approximation. Figure 17(b) shows that the spherical approximation for the rising velocity starts to be-

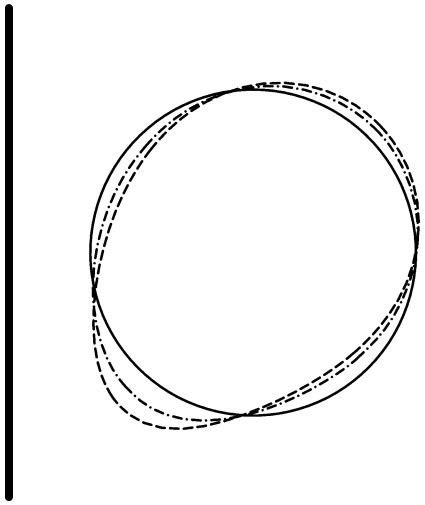

FIG. 18. Time evolution of the droplet profile (i.e., the intersection of the droplet interface with the plane $y=0$) for $B_d=3$, $\lambda=1$, and $(x_{c0},z_{c0})=(0,1.5)$ at different times: ——, $t=0$; ----, $t=20$; -·-, $t=90$. The corresponding location of the drop centroid (with increasing time) is $x_c\approx 0,3.74,17.63$ and $z_c\approx 1.5,1.61,2.02$. The profiles are aligned at the initial location to demonstrate the interfacial deformation.

come valid after a distance of a few only drop radii from the wall, as predicted in Ref. 23. It is of interest to note that based on the spherical approximation, one can show that the droplet obtains its maximum rising velocity (i.e., that in an unbounded fluid) in a distance from the wall about 20–30 times the characteristic drop radius. Due to its slow migration speed, this means that the droplet needs to travel a significant vertical distance until it is not affected by the presence of the wall.

To show the evolution of the interfacial shape, in Fig. 18 we plot the droplet profile (i.e., the intersection of the droplet interface with the plane $y=0$) for $B_d=3$ and $\lambda=1$ at three different times $t=0,20,90$. The initial spherical shape has been deformed (and rotated) at its maximum deformation near time $t=20$; later the drop shows a slow relaxation toward its undisturbed shape as it migrates slowly away from the wall.

We now turn our attention to the time evolution of the droplet deformation D for several Bond numbers shown in Fig. 19(a). Note that we calculate D via Eq. (22) based on the droplet semiaxes determined as the maximum and minimum distance from the droplet's centroid. For the asymmetric shapes of a drop moving near a solid wall, the deformation parameter D we present in this section may differ from that based on the droplet's maximum and minimum lengths. Figure 19(a) reveals that the interfacial deformation shows an initial fast increase followed by a slow decrease toward its zero value far from the wall while by increasing the buoyant effects (or B_d), the drop shows increased deformation. We note that the time evolution of the drop deformation D is quite similar to that of the migration velocity U_z presented in Fig. 15(b), which verifies that the droplet's lateral motion is deformation induced under Stokes flow conditions.[23,43] To show the evolution of the drop's orientation, in Fig. 19(b) we plot the orientation angle θ_x of the drop's major semiaxis L with respect to the negative x axis. Observe that the spherical

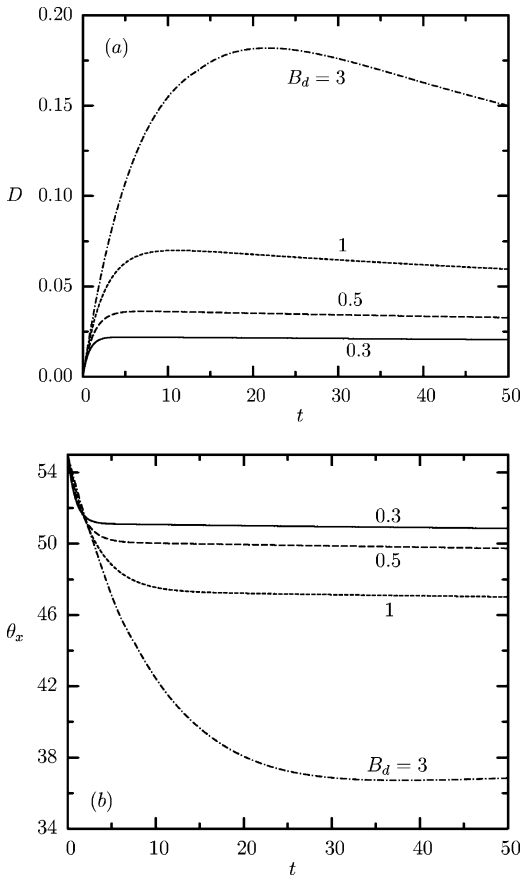

FIG. 19. Time evolution of the deformation of a droplet with $\lambda=1$ for Bond number $B_d=0.3,0.5,1,3$. (a) Deformation parameter D. (b) Orientation angle θ_x of the drop's major semiaxis L with respect to the negative x axis. The initial drop location is $z_{c0}=1.5$.

droplet, immediately after left near the solid wall to rise, shows an initial large rotation, corresponding to $\theta_x\approx 55°$, independent of the Bond number. The drop orientation then decreases fast while later the drop shows a very slow change in orientation toward its final configuration far from the wall.

The droplet deformation D as a function of its lateral position z_c for different Bond numbers is shown in Fig. 20.

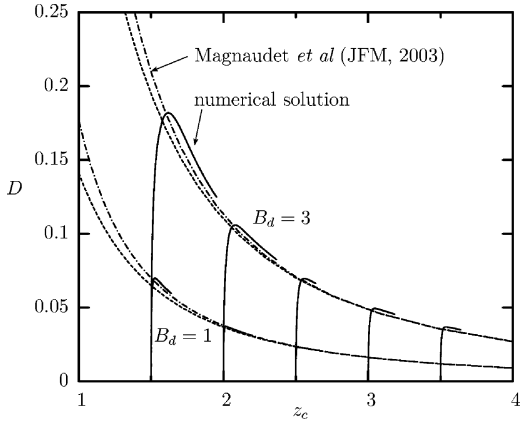

FIG. 20. Deformation D versus lateral position z_c for a droplet with $\lambda=1$ and for Bond number $B_d=1,3$. The initial drop location is $z_{c0}=1.5,2,2.5,3,3.5$. Also included are the analytical predictions for D of $O(z_c^{-3})$ (----) and $O(z_c^{-5})$ (-·-) from Ref. 23.

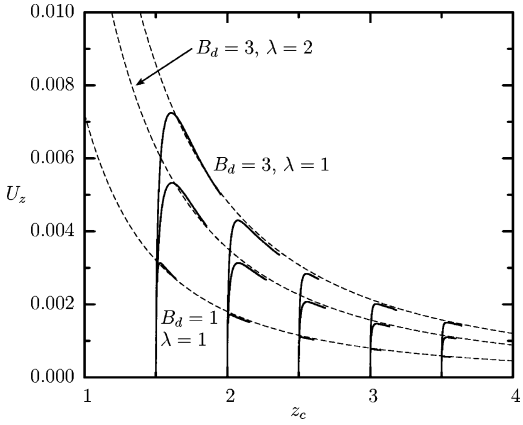

FIG. 21. Migration velocity U_z versus lateral position z_c for a droplet with $\lambda=1,2$ and for Bond number $B_d=1,3$. The initial drop location is $z_{c0}=1.5,2,2.5,3,3.5$. Also included is the best z_c^{-2} fitting (---) based on the decreasing velocity.

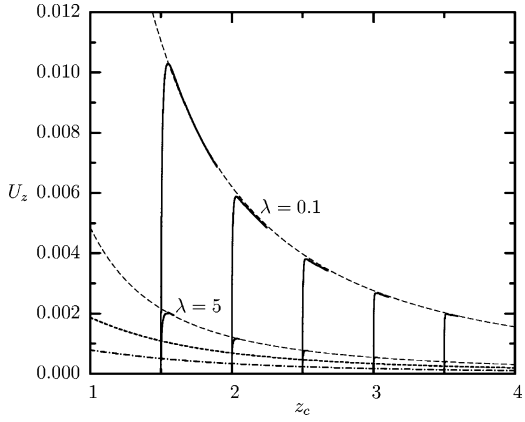

FIG. 22. Migration velocity U_z versus lateral position z_c for a droplet with $B_d=1$ and for $\lambda=0.1,5$: numerical results (solid lines) and best z_c^{-2} fitting (– – –) based on the decreasing velocity. The initial drop location is $z_{c0}=1.5,2,2.5,3,3.5$. Also included are the analytical predictions for U_z for $\lambda=0.1$ (----) and $\lambda=5$ (-·-) from Ref. 23.

The initially spherical droplet shows a significant deformation at first without any substantial lateral migration while the droplet deformation increases with the Bond number. After the maximum deformation has been reached the droplet shows a slow relaxation toward its spherical shape as it migrates away from the wall. In Fig. 20 we also include the analytical predictions for the drop deformation of $O(z_c^{-3})$ and $O(z_c^{-5})$ by employing Eqs. (14b) and (18) from Ref. 23. [Note that for the analytical prediction of $O(z_c^{-5})$, the terms denoted as M_4 and M_5 have not been provided in Ref. 23 due to the complexity to be derived algebraically and their expected limited contribution; this is the reason that we include both analytical predictions in our Fig. 20.] The analytical results for D agree very well with the numerical calculations as the distance from the wall increases and/or the Bond number decreases.

We conclude our investigation of the buoyant drop motion by considering the migration velocity U_z as a function of its lateral position z_c for different Bond numbers and viscosity ratios. As shown in Fig. 21, the dependence of U_z on z_c is quite similar to that for the interfacial deformation D shown in Fig. 20. After the spherical droplet is left close to the solid wall, its lateral migration is almost negligible until the shape has reached its maximum deformation and thus obtained its maximum migration velocity. Afterward, the droplet moves away from the wall while both its deformation and its migration velocity show a slow relaxation toward zero far from the wall. The deformation and migration velocity are higher for a larger Bond number (for a given viscosity ratio); on the other hand, for a given Bond number, the more viscous droplet shows a smaller migration velocity. In Fig. 21 we also include the best z_c^{-2} fitting based on the decreasing velocity. Observe that during relaxation, the migration velocity decreases inversely with the square of the lateral position for all cases studied, as commonly found in drop motion near solid walls.[43]

The recent analytical study of Magnaudet, Takagi, and Legendre[23] predicts the z_c^{-2} dependence of the migration velocity U_z; however, it also predicts that the droplet should move away or toward the solid wall based on the viscosity ratio. In particular, the first-order analysis in B_d given by Eq. (36) in the analytical study[23] predicts that the droplet moves toward the wall for $0.21 \approx (5-19^{1/2})/3 < \lambda < (5+19^{1/2})/3 \approx 3.12$, while it migrates away otherwise. We note that the migration analysis is formally valid for $\lambda B_d \ll 1$; however, it is expected to be practically valid for $\lambda B_d \leqslant 1$, as discussed in Sec. 3.2 in Ref. 23. (For example, the analytical predictions for the droplet deformation D are in very good agreement with our computational results, as shown in Fig. 20 for $B_d=1,3$, and $\lambda=1$.) Our numerical results presented in Figs. 15(b) and 21 show that the analytical prediction of lateral motion toward the wall is erroneous, at least for the Bond numbers studied in this paper ($B_d \geqslant 0.3$).

To see how well the predictions of the analytical work[23] match the migration velocity for the range of the viscosity ratios it predicts a lateral motion away from the wall, in Fig. 22 we compare our numerical results with the analytical predictions for a droplet with $B_d=1$ and for $\lambda=0.1,5$. Note that our results show that the migration velocity decreases inversely with the square of the lateral position. In addition our computations reveal that the analytical study of Magnaudet, Takagi, and Legendre[23] underestimates the migration velocity away from the solid wall (for the parameter space we studied in this paper).

Therefore, the major conclusion of this section is that analytical models[23] predict quite well the rising velocity and the deformation of droplets near solid walls for $\lambda=O(1)$ and Bond number $B_d=O(1)$. However, they underestimate the migration velocity away from the wall or erroneously predict lateral motion toward the solid wall in the same range of the parameter space. Our finding about the inability of the analytical models to predict the correct migration velocity is in agreement with the results of Uijttewaal and Nijhof[48] who via computations showed that analytical models overestimate the migration velocity in the case of droplet motion in shear flow near a solid wall.

VII. CONCLUSIONS

In this paper we have described a spectral boundary integral approach for interfacial dynamics in three-dimensional Stokes flow. To preserve the continuity of the interfacial geometry and its derivatives at the edges of the spectral elements during the droplet deformation, a suitable interfacial smoothing based on a Hermitian-like interpolation has been developed. Our smoothing methodology preserves the main characteristic of the spectral methods, i.e., the exponential convergence in the interfacial accuracy as the number of spectral points increases. The accuracy of the method and the associated exponential convergence have been demonstrated for the calculation of the geometric properties of a given shape, such as the interfacial curvature, as well as the dynamic evolution of the interfacial shape. An adaptive mesh reconstructing procedure based on relevant lengths of the spectral elements has also been described.

Our investigation of the inertialess motion of a buoyant droplet left to rise (or sediment) near a vertical solid wall reveals the strengths and the shortcomings of relevant analytical models. In particular, our work shows that the analytical study of Magnaudet, Takagi, and Legendre[23] predicts quite well the rising velocity and interfacial deformation but underestimates the migration velocity away from the wall or erroneously predicts lateral motion toward the solid wall, for the range of parameter space included in our study, i.e., for viscosity ratio $\lambda = O(1)$ and Bond number $B_d = O(1)$. Therefore, our work emphasizes the need for computational studies for the accurate determination of droplet migration near solid walls.

The present algorithm constitutes a new approach for interfacial dynamics in Stokes flow based on the (high-order) spectral boundary element formulation that in the near past has demonstrated its high accuracy, robustness, and efficiency for fixed boundary surfaces,[14–16] particulate flows,[17] and equilibrium interfaces under steady flows and/or gravity.[18–22] Thus, it can be employed for a wide range of interfacial problems in porous media, microfluidic devices, and physiological systems.

ACKNOWLEDGMENTS

This work was supported in part by the National Science Foundation (Grant No. CTS-0218770). Acknowledgment is made to the Donors of the American Chemical Society Petroleum Research Fund for partial support of this research. Some computations were performed on multiprocessor computers provided by the National Center for Supercomputing Applications Applications (NCSA) in Illinois.

[1] G. K. Youngren and A. Acrivos, "On the shape of a gas bubble in a viscous extensional flow," J. Fluid Mech. **76**, 433 (1976).
[2] J. M. Rallison, "The deformation of small viscous drops and bubbles in shear flows," Annu. Rev. Fluid Mech. **16**, 45 (1984).
[3] H. A. Stone, "Dynamics of drop deformation and breakup in viscous fluids," Annu. Rev. Fluid Mech. **26**, 65 (1994).
[4] C. Pozrikidis, "Interfacial dynamics for Stokes flow," J. Comput. Phys. **169**, 250 (2001).
[5] C. Pozrikidis, in *Modeling and Simulation of Capsules and Biological Cells* (Chapman & Hall, London, 2003).
[6] A. Z. Zinchenko and R. H. Davis, "Shear flow of highly concentrated emulsions of deformable drops by numerical simulations," J. Fluid Mech. **455**, 21 (2002).
[7] J. M. Rallison, "A numerical study of the deformation and burst of a viscous drop in general shear flows," J. Fluid Mech. **109**, 465 (1981).
[8] M. Loewenberg and E. J. Hinch, "Numerical simulation of a concentrated emulsion in shear flow," J. Fluid Mech. **321**, 395 (1996).
[9] A. Z. Zinchenko, M. A. Rother, and R. H. Davis, "A novel boundary-integral algorithm for viscous interaction of deformable drops," Phys. Fluids **9**, 1493 (1997).
[10] I. B. Bazhlekov, P. D. Anderson, and H. E. H. Meijer, "Nonsingular boundary integral method for deformable drops in viscous flows," Phys. Fluids **16**, 1064 (2004).
[11] C. Canuto, M. Y. Hussaini, A. Quarteroni, and T. A. Zang, *Spectral Methods in Fluid Dynamics* (Springer-Verlag, New York, 1998).
[12] M. Y. Hussaini and T. A. Zang, "Spectral methods in fluid dynamics," Annu. Rev. Fluid Mech. **19**, 339 (1987).
[13] Y. Maday and A. T. Patera, "Spectral element methods for the incompressible Navier-Stokes equations," in *State of the Art Surveys in Computational Mechanics*, edited by A. K. Noor and J. T. Oden (ASME, New York, 1989).
[14] J. M. Occhialini, G. P. Muldowney, and J. J. L. Higdon, "Boundary integral/spectral element approaches to the Navier-Stokes equations," Int. J. Numer. Methods Fluids **15**, 1361 (1992).
[15] G. P. Muldowney and J. J. L. Higdon, "A spectral boundary element approach to three-dimensional Stokes flow," J. Fluid Mech. **298**, 167 (1995).
[16] J. J. L. Higdon and G. P. Muldowney, "Resistance functions for spherical particles, droplets and bubbles in cylindrical tubes," J. Fluid Mech. **298**, 193 (1995).
[17] C. Pozrikidis, "A spectral-element method for particulate Stokes flow," J. Comput. Phys. **156**, 360 (1999).
[18] P. Dimitrakopoulos and J. J. L. Higdon, "Displacement of fluid droplets from solid surfaces in low-Reynolds-number shear flows," J. Fluid Mech. **336**, 351 (1997).
[19] P. Dimitrakopoulos and J. J. L. Higdon, "On the displacement of three-dimensional fluid droplets from solid surfaces in low-Reynolds-number shear flows," J. Fluid Mech. **377**, 189 (1998).
[20] P. Dimitrakopoulos and J. J. L. Higdon, "On the gravitational displacement of three-dimensional fluid droplets from inclined solid surfaces," J. Fluid Mech. **395**, 181 (1999).
[21] P. Dimitrakopoulos and J. J. L. Higdon, "On the displacement of three-dimensional fluid droplets adhering to a plane wall in viscous pressure-driven flows," J. Fluid Mech. **435**, 327 (2001).
[22] P. Dimitrakopoulos and J. J. L. Higdon, "On the displacement of three-dimensional fluid bridges from solid surfaces in viscous pressure-driven flows," Phys. Fluids **15**, 3255 (2003).
[23] J. Magnaudet, S. Takagi, and D. Legendre, "Drag, deformation and lateral migration of a buoyant drop moving near a wall," J. Fluid Mech. **476**, 115 (2003).
[24] C. Pozrikidis, *Boundary Integral and Singularity Methods for Linearized Viscous Flow* (Cambridge University Press, Cambridge, 1992).
[25] M. Abramowitz and I. A. Stegun, in *Handbook of Mathematical Functions with Formulas, Graphs, and Mathematical Tables* (Dover, New York, 1972).
[26] M. Loewenberg and E. J. Hinch, "Collision of two deformable drops in shear flow," J. Fluid Mech. **338**, 299 (1997).
[27] V. Cristini, J. Blawzdziewicz, and M. Loewenberg, "An adaptive mesh algorithm for evolving surfaces: simulations of drop breakup and coalescence," J. Comput. Phys. **168**, 445 (2001).
[28] A. Z. Zinchenko and R. H. Davis, "A multipole-accelerated algorithm for close interaction of slightly deformable drops," J. Comput. Phys. **207**, 695 (2005).
[29] R. H. Davis, "Buoyancy-driven viscous interaction of a rising drop with a smaller trailing drop," Phys. Fluids **11**, 1016 (1999).
[30] P. Dimitrakopoulos, "Computational studies of droplet displacement in Stokes flow," M.S. thesis, University of Illinois, 1996.
[31] S. Kwak and C. Pozrikidis, "Adaptive triangulation of evolving, closed, or open surfaces by the advancing-front method," J. Comput. Phys. **145**, 61 (1998).
[32] B. J. Bentley and L. G. Leal, "An experimental investigation of drop deformation and breakup in steady, two-dimensional linear flows," J. Fluid Mech. **167**, 241 (1986).
[33] S. Guido and M. Villone, "Three-dimensional shape of a drop under simple shear flow," J. Rheol. **43**, 395 (1998).
[34] G. I. Taylor, "The viscosity of a fluid containing small drops of another

fluid," Proc. R. Soc. London, Ser. A **138**, 41 (1932).
[35] Y. Wang, "Numerical studies of Stokes flow in confined geometries," M.S. thesis, University of Maryland, 2004.
[36] J. W. Ha and L. G. Leal, "An experimental study of drop deformation and breakup in extensional flow at high capillary number," Phys. Fluids **13**, 1568 (2001).
[37] A. J. Goldman, R. G. Cox, and H. Brenner, "Slow viscous motion of a sphere parallel to a plane wall. Part I. Motion through a quiescent liquid," Chem. Eng. Sci. **22**, 637 (1967).
[38] M. E. O'Neill and K. Stewarson, "On the slow motion of a sphere parallel to a nearby plane wall," J. Fluid Mech. **27**, 706 (1967).
[39] P. Vasseur and R. G. Cox, "The lateral migration of spherical particles sedimenting in a stagnant bounded fluid," J. Fluid Mech. **80**, 561 (1977).
[40] L. G. Leal, "Particle motions in a viscous fluid," Annu. Rev. Fluid Mech. **12**, 435 (1980).
[41] F. Takemura, "Migration velocities of spherical solid particles near a vertical wall for Reynolds number for 0.1 to 5," Phys. Fluids **16**, 204 (2004).
[42] L. Zeng, S. Balachandar, and P. Fischer, "Wall-induced forces on a rigid sphere at finite Reynolds number," J. Fluid Mech. **536**, 1 (2005).
[43] P. C.-H. Chan and L. G. Leal, "The motion of a deformable drop in a second-order fluid," J. Fluid Mech. **92**, 131 (1979).
[44] M. Shapira and S. Haber, "Low Reynolds number motion of a droplet between two parallel plates," Int. J. Multiphase Flow **14**, 483 (1988).
[45] M. Shapira and S. Haber, "Low Reynolds number motion of a droplet in shear flow including wall effects," Int. J. Multiphase Flow **16**, 305 (1990).
[46] J. R. Smart and D. T. Leighton, Jr., "Measurement of the drift of a droplet due to the presence of a plane," Phys. Fluids A **3**, 21 (1991).
[47] W. S. J. Uijttewaal, E. J. Nijhof, and R. M. Heethaar, "Droplet migration, deformation, and orientation in the presence of a plane wall: A numerical study compared with analytical theories," Phys. Fluids A **5**, 819 (1993).
[48] W. S. J. Uijttewaal and E. J. Nijhof, "The motion of a droplet subjected to linear shear flow including the presence of a plane wall," J. Fluid Mech. **302**, 45 (1995).
[49] F. Takemura, S. Takagi, J. Magnaudet, and Y. Matsumoto, "Drag and lift forces on a bubble rising near a vertical wall in a viscous liquid," J. Fluid Mech. **461**, 277 (2002).
[50] F. Takemura and J. Magnaudet, "The transverse force on clean and contaminated bubbles rising near a vertical wall at moderate Reynolds number," J. Fluid Mech. **495**, 235 (2003).
[51] S. D. Hudson, "Wall migration and shear-induced diffusion of fluid droplets in emulsions," Phys. Fluids **15**, 1106 (2003).
[52] T. D. Taylor and A. Acrivos, "On deformation and drag of a falling viscous drop at low Reynolds number," J. Fluid Mech. **18**, 466 (1964).